npj | materials degradation

Article

Published in partnership with CSCP and USTB

https://doi.org/10.1038/s41529-026-00800-0

The effect of deformation-induced cracks on the corrosion behaviour of HDG Zn-Mg-Al coatings

A. D. Malla[1] ✉, D. J. Penney[1], G. Williams[1], F. E. Goodwin[2], Ana P. Domingos Cardoso[3], M. Brooks[1] & J. H. Sullivan[1]

Zn-Mg-Al coatings (ZMA) on steel can provide enhanced corrosion resistance compared to zinc coating (GI) and are often used in applications that require shaping processes. This study investigates the effect of deformation-induced cracking on the corrosion of ZMA coatings of different weights (310 and 80 g m^{-2}) benchmarked against GI. Cracks were more prevalent and of greater depth in ZMA coatings due to the presence of $MgZn_2$ in the eutectic. ZMA with 310 g m^{-2} weight (ZMA310), exhibited a ~ 3 times greater crack area than 80 g m^{-2} weight (ZMA80) through an increased eutectic volume fraction. This caused an increase in corrosion rate of 3.8 times for ZMA310 relative to its undeformed condition over 24 h, with increases between 1.5 and 1.7 times for ZMA80 and GI. Two phenomena cause this increase: deformation-accelerated corrosion due to differential aeration-induced anodic activation in non-through-coating cracks, and cathodic activation in through-coating cracks resulting from galvanic coupling with the steel.

Hot-dip galvanising (HDG) is a widely used surface treatment process that delays the corrosion of steel structures and prolongs their service life. The enhanced corrosion resistance is due to the presence of a metallic zinc/zinc alloy coating applied to both sides of the steel which provides both barrier and cathodic protection. Conventional hot-dip galvanised metallic coatings are based on zinc (Zn, also termed GI coatings) but can also be zinc alloys containing aluminium or aluminium and magnesium to improve performance. Hot-dip galvanised steels (HDGS's) are employed in numerous outdoor and indoor applications across diverse industries. Consequently, they often undergo shaping processes such as pressing, stamping, roll forming and bending to achieve the desired shapes and profiles. These processes can induce large deformations to the steel substrate and the metallic coatings. The deformations are complex due to the differences in the mechanical properties of the substrate and the HDG coatings. Ideally, the coatings must be ductile enough to form without fracturing or separating from the steel substrate; hence, formability and good cracking resistance are of paramount importance. The coating ductility depends on numerous factors such as thickness, phase compositions, intermetallic layer, grain size and crystallographic orientations[1]. Nonetheless, the profiling processes can induce cracks in the HDG coatings[2]. The presence of defects such as cracks provides a passage for oxygen and moisture, consequently degrading the corrosion protection afforded by the coatings[3,4]. Therefore, deformation-induced cracks on HDG coatings have been a constant concern.

Zinc-magnesium-aluminium (Zn-Mg-Al) (ZMA) alloy coatings, which show significantly enhanced corrosion resistance[5–9], have accelerated the interest in coating formability on account of these alloys exhibiting higher hardness compared to standard GI coatings[10]. The enhanced corrosion resistance of ZMA coatings has been attributed to their unique microstructure[6,11,12]. ZMA coatings produced via continuous HDG exhibit anisotropic microstructures comprising primary Zn, coarser lamellar binary eutectic (Zn + $MgZn_2$) and fine ternary eutectic (Zn + $MgZn_2$ + Al nodules) phases[13,14]. Despite improved corrosion resistance, the crack resistance of ZMA coatings is inferior to that of GI[15,16] and Zn-Al[17]. Under deformation, HDG Zn demonstrates intergranular cracking in contrast to transgranular cracking for ZMA[1,18–20]. This transgranular cracking has been attributed to insufficient slip systems[21]. The intermetallic $MgZn_2$ phase present in the binary eutectic phase has been reported as the source of the crack initiation site[22]. Hence, the modification of the microstructure, removal of the binary eutectic phase, refinement of the primary Zn phase and the modification of crystallographic texture have proven to enhance the crack resistance of ZMA[16,18,23].

The corrosion behaviour of flat ZMA surfaces has been rigorously studied[8,13,24–33] however, investigations on deformed ZMA surfaces are less common. Some investigations have been conducted on the profiled surfaces

[1]Corrosion and Coatings Group, School of Engineering and Applied Sciences, Swansea University, Bay Campus, Fabian Way, Crymlyn Burrow, Swansea, UK. [2]International Zinc Association, Durham, NC, USA. [3]International Zinc Association, Brussels, Belgium. ✉e-mail: amar.malla@swansea.ac.uk

of stainless steel[34], galvanneal steel[35], GI[36], Zn-Al[4], electrogalvanized steel[3] and deterioration of corrosion resistance has been reported in all cases. Given this, it is important to investigate the influence of deformation on the protective ability of HDG ZMA coatings.

This investigation provides insights into the corrosion performance of deformed ZMA coatings as a function of their coating weight. The effect of coating weights (thicknesses) on the surface and cut-edge corrosion behaviour of undeformed ZMA coatings has been reported previously[37]. In this new study, a structural grade steel substrate commonly used in construction, coated with ZMA coating, was bent to 45°. The resultant surface area was analysed using a Keyence Microscope for surface crack analysis. The corrosion performance of deformed ZMA coatings with different coating weights (thickness) in pH 7 0.17 M NaCl was investigated. DC electrochemistry [Open Circuit Potential (OCP) and Linear Polarisation Resistance (LPR)] and the scanning vibrating electrode technique (SVET) were used to assess the corrosion performance. Additionally, GI was investigated as stated, serving as the benchmark.

Results

Materials characterisation

The continuous galvanising line produced ZMA coatings with different weights, as well as a GI coating investigated in this study, are presented in Table 1.

The microstructure of ZMA is multi-phased: primary Zn, binary lamellar eutectic (Zn and $MgZn_2$) and ternary lamellar eutectic (Zn, $MgZn_2$ and Al nodules)[27,38]. The morphology, volume fraction, and distribution of these constituents are influenced by the processing parameters, such as coating weight/thickness[37], bath chemistry[39] and cooling rate[13]. Images of HDG GI and ZMA coating with coating weights of 80 $g.m^{-2}$ and 310 $g.m^{-2}$ are presented in Fig. 1. Figure 1a–c shows the surface microstructure, and Fig. 1d–f shows the through-coating microstructure. The GI demonstrated a single-phase microstructure, whereas ZMA80 and ZMA310 demonstrated a multiphase microstructure. Furthermore, a significant difference in the microstructure morphology is observed between the thinner ZMA80 and the thicker ZMA310. ZMA80 demonstrated fine microstructure with globular-shaped primary Zn phases surrounded by eutectic phases. ZMA310 demonstrated a coarser microstructure with large dendritic primary Zn phases. Numerous straight-through coating eutectic pathways from the coating surface to the steel substrate could be observed in ZMA80 (Fig. 1e). In contrast, the thicker ZMA310 exhibits a more tortuous pathway due to the presence of dendritic primary Zn phases (Fig. 1f).

Table 2 presents the volume fraction of the primary Zn phase and the summed total of the two eutectic phases of both ZMA80 and ZMA310. The errors are based on the standard deviation of five measurements. The table also presents the coating thickness of the coatings under investigation. The coating thickness was measured using cut-edge SEM images. The errors shown are based on the standard deviation of ten measurements. The volume fraction of the primary Zn phase and the eutectic phase varied with increasing coating weight. The volume fraction of the primary Zn phase decreased from 82.3% to 68.5%, whereas the eutectic phase increased from 17.8% to 31.5% when the ZMA coating weight increased from 80 $g.m^{-2}$ (ZMA80) to 310 $g.m^{-2}$ (ZMA310). The measured coating thickness per side for GI, ZMA80 and ZMA310 was 25 µm, 6.9 µm and 27 µm, respectively.

Effect of deformation on HDG coatings

The steel substrate coated with HDG GI and ZMA coatings was subject to bending deformation at 45°, 90°, 135° and 180° angles. Surface crack area as a function of bend angle for HDG GI and ZMA is presented in Fig. 2. It shows that the surface crack area increases with an increase in strain, i.e., the bend angle. However, the increase in surface crack area is much greater for ZMAs compared to GI. Among the ZMAs, the thicker ZMA310 showed a higher

Table 1 | The samples with various coating weights under investigation

Sample	Coating weight ($g.m^{-2}$)	Zn (wt%)	Mg (wt%)	Al (wt%)
GI	275	99.80	0	0.2
ZMA80	80	96-98	1-2	1-2
ZMA310	310	96-98	1-2	1-2

Table 2 | Coating thickness, average primary Zn phase and total eutectic phase volume fractions for different coatings

Sample	Zn phase volume (%)	Total eutectic phase volume (%)	Coating thickness per side (µm)
GI	100	-	25 ± 1.15
ZMA80	82.3 ± 2.6	17.8 ± 2.6	6.9 ± 1.1
ZMA310	68.5 ± 7.3	31.5 ± 7.3	27.1 ± 1.5

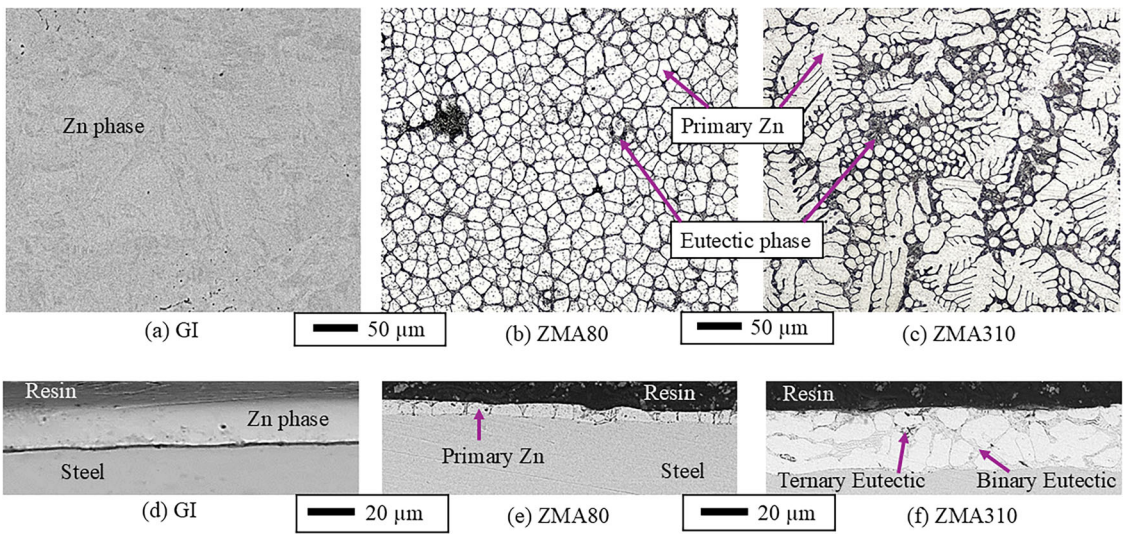

Fig. 1 | Images showing the microstructure of HDG coatings. a–c shows the surface microstructure, and **d–f** shows the cut-edge microstructure of HDG GI and ZMA coatings obtained using SEM. The primary Zn phases have transformed from a globular to a dendritic structure with the change in ZMA coating weight from 80 $g.m^{-2}$ to 310 $g.m^{-2}$.

surface crack area compared to the thinner ZMA80 for all tested bend angles. For all bend angles, the surface crack area was in the order ZMA310 > ZMA80 > GI.

Due to the limitations[40] of one of the techniques (SVET) used in this investigation, only surfaces subjected to a 45° bend were selected for corrosion investigations and hence, these 45° bend samples are further discussed here. Figure 3 shows the cracks formed on the surface after a 45° bend and the area of the samples used for surface crack analysis and corrosion experiments. In Fig. 3, the surface crack areas have been highlighted and coloured green. The figure indicates that the crack area percentage in ZMA310 is significantly greater than that observed in ZMA80 following 45° bends.

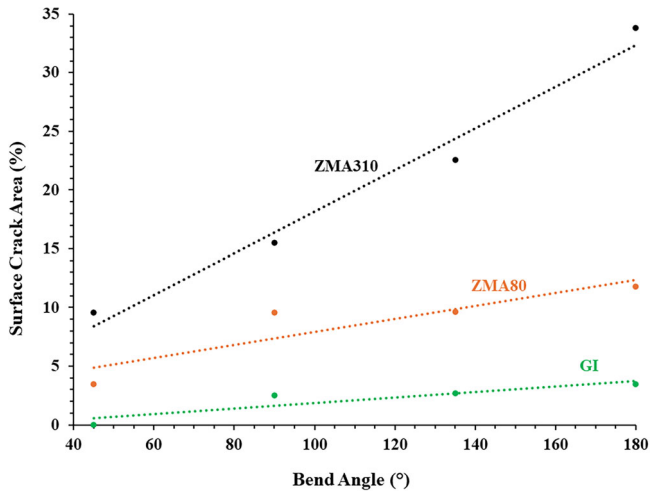

Fig. 2 | The effect of bend angles on the surface crack area for the different coatings. The surface crack area increases with the increase in the bend angle.

The surface crack area (%) at 45° bend for all three coatings is presented in Table 3. For GI, the surface crack area (%) is very low, i.e. 0.6%. However, ZMA coatings demonstrated significantly higher values. The ZMA310 coating has ~ 16 times the crack area of the GI and ~ 3 times the crack area of ZMA80.

Investigation of corrosion behaviour of flat and formed galvanised coatings

The SVET was utilised to investigate the surface corrosion behaviour of GI and ZMA coatings in a 0.17 M NaCl pH 7 solution over 24 h. The normal current density measured above freely corroding flat surfaces of GI, ZMA80 and ZMA310 at 1 h, 6 h, 12 h, 18 h, and 24 h is presented in Fig. 4. The anodic and cathodic activities are shown as red and blue, respectively. The SVET provides a visual representation of the location and intensity of anodic and cathodic activities, as registered by the SVET probe. For all three coatings, after 1 h of corrosion testing, anodes were apparent on the surfaces; however, a difference in the anode growth mechanism was observed for ZMA80 compared to GI and ZMA310. For ZMA80, the anode established at 1 h (ii, marked on 1 h SVET colour map, Fig. 4) grew radially, forming a ring or hollow shape, suggesting that anodic deactivation occurs as the anodic front grows. This phenomenon is not observed for ZMA310 and GI. For example, the anode marked (i) on the 1 h SVET colour map, Fig. 4, does not form a ring or hollow shape as the time progresses. In addition, the

Table 3 | Surface crack area (%) measured at 45° bend surfaces for different coatings under investigation

Sample	Surface crack area (%)
GI	0.6
ZMA80	3.1
ZMA310	9.6

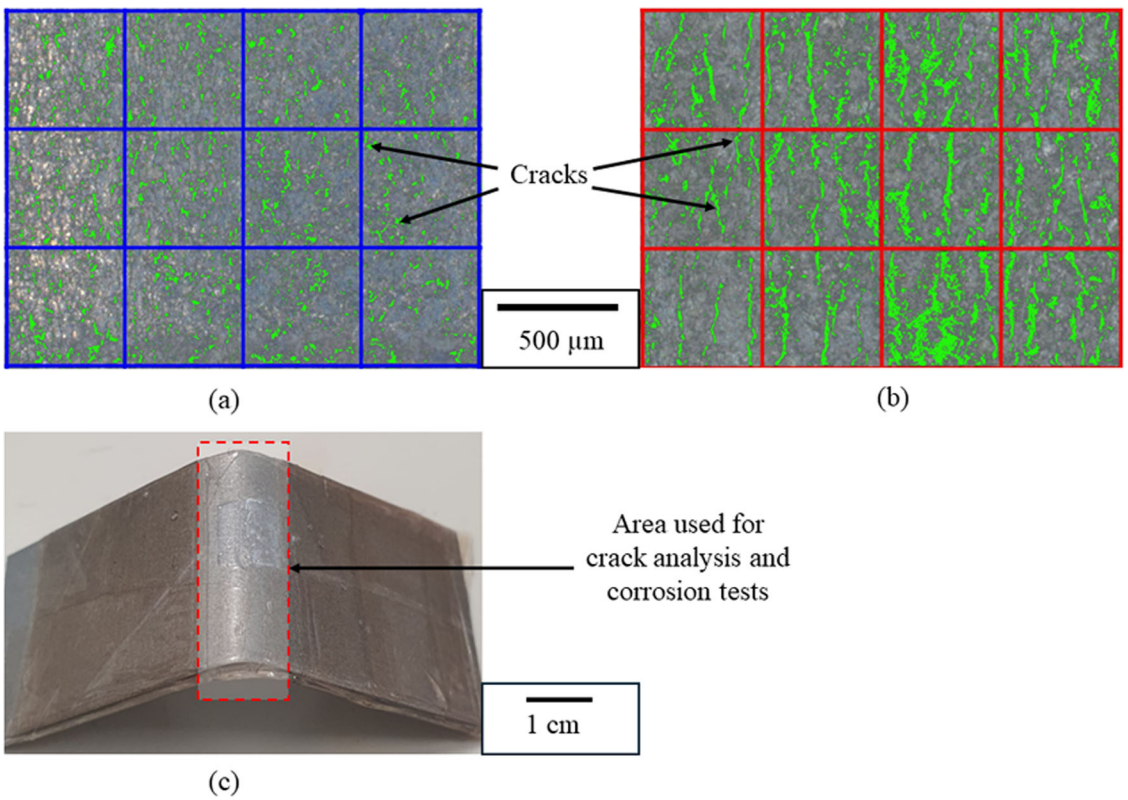

Fig. 3 | Illustration of colour data for measuring the surface cracked area of ZMA coatings. a, b shows the cracks formed on ZMA80 and ZMA310 respectively, after a 45° bend. **c** shows the area used for crack analysis and corrosion experiments. The number of cracks on the surface increases with the increase in coating weight.

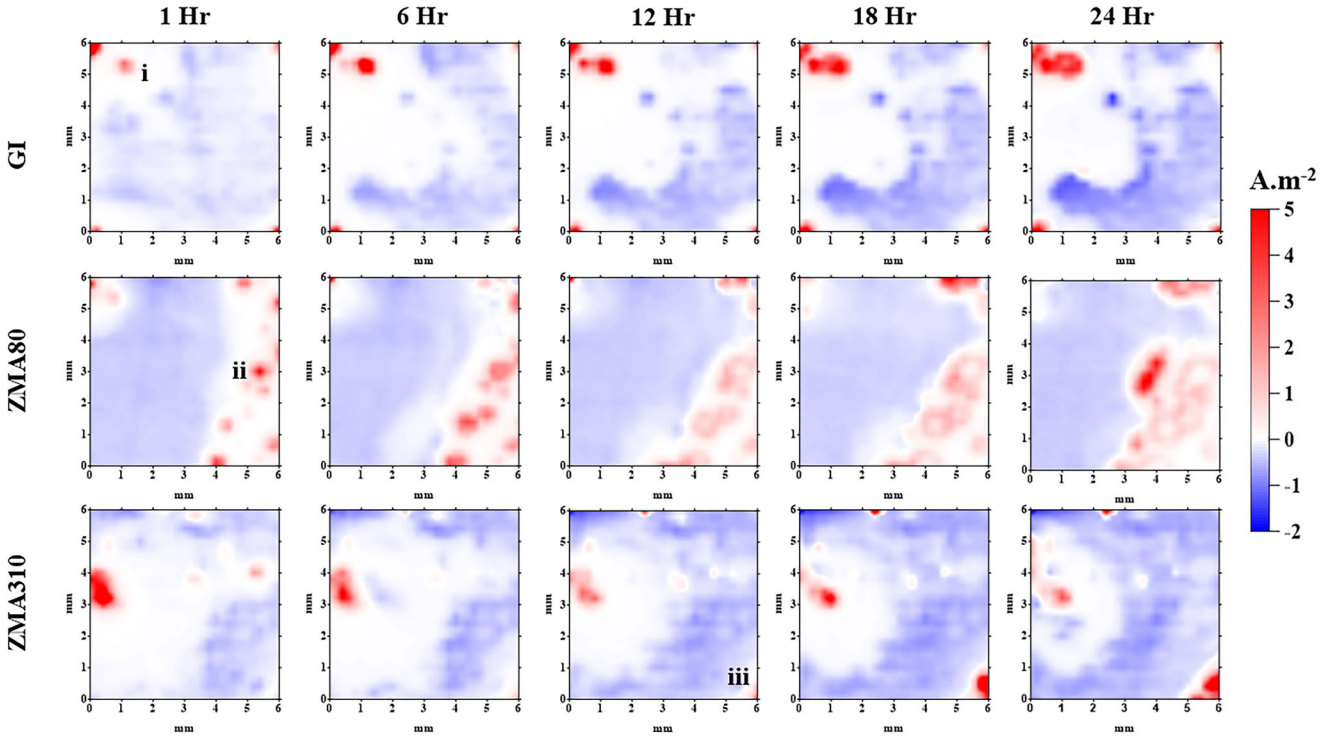

Fig. 4 | SVET colour maps representing normal current density measured above freely corroding GI and ZMA surfaces immersed in a 0.17 M NaCl, pH 7 solution for 24 h. The colour maps presented are 1 h, 6 h, 12 h, 18 h and 24 h of immersion time for GI and ZMA surfaces.

Table 4 | SVET-derived metal loss for flat surfaces of GI, ZMA80 and ZMA310 after immersion in 0.17 M NaCl pH 7 solution for 24 h

Sample	Flat Surface ($g.m^{-2}$)
ZMA80	6.69 ± 1.75
ZMA310	2.40 ± 1.15
GI	6.74 ± 0.71

number of anodic features is greater on the ZMA80 surface compared to ZMA310 and GI.

The SVET-derived 24-hour cumulative metal losses for GI, ZMA80 and ZMA310 after immersion in pH 7 0.17 M NaCl are presented in Table 4. The errors shown are based on the standard deviation of two measurements. GI and ZMA80 demonstrated similar metal losses of 6.74 $g.m^{-2}$ and 6.69 $g.m^{-2}$, respectively, whereas ZMA310 demonstrated a metal loss of 2.40 $g.m^{-2}$. For ZMA, increasing the coating weight from 80 $g.m^{-2}$ to 310 $g.m^{-2}$ has significantly improved corrosion resistance, as SVET-derived metal loss decreased by 64% from 6.69 $g.m^{-2}$ to 2.40 $g.m^{-2}$.

To evaluate the effect of deformation-induced cracks on corrosion behaviour, formed samples were investigated using the SVET and DC electrochemistry. Each galvanised coating was bent to an angle of 45° and an area of 6 × 6 mm scanned encompassing the peak of the bend (shown in Fig. 3c). Figure 5 shows the height profile of the formed GI measured by the SVET, along with illustrative normal current density maps recorded at 1 h, 6 h, 12 h, 18 h and 24 h in a 0.17 M NaCl pH 7 solution. In Fig. 5, anodic and cathodic activities are shown in red and blue colours, respectively. Peak normal current densities of 5 $A.m^{-2}$ were recorded. Figure 5 shows that anodic activities were focused on the peak/bend of the formed surface, whereas the cathodic activities were concentrated on the area away from the peak (bend). The band of anodic activitiy detected at 1 h and 6 h has shrunk, and some individual localised anodes could be observed on 12 h and 18 h.

Figure 6 shows the height profile of the formed ZMA80 measured by the SVET, along with illustrative normal current density maps recorded at 1 h, 6 h, 12 h, 18 h and 24 h in a 0.17 M NaCl pH 7 solution. In contrast to GI, the formed ZMA80 surface height map shows some irregularities, potentially cracks caused by a 45° bend. For ZMA80, the 1 h and 6 h SVET colour maps suggested that the anodic activities were concentrated on the very bend and its vicinity, similar to GI. However, from 12 h onwards, anodic activities were detected in areas other than the bend in addition to the bend area. By 24 h, the anodic activity was concentrated at the irregularities detected during the height map scan.

Figure 7 shows the height profile of the formed ZMA310 measured by the SVET, along with illustrative normal current density maps measured at 1 h, 6 h, 12 h, 18 h and 24 h in a 0.17 M NaCl pH 7 solution. In contrast to GI and similar to ZMA80, the formed ZMA310 surface height map also shows irregularities (along the y-axis direction), potentially cracks caused by a 45° bend. Similar to GI and ZMA80, the anodic activities are concentrated at the bend surface and its vicinity. However, towards the end of the experiment, the anodic activities is concentrated on the bend surface, along with the irregularities detected during the height map scan.

The time-dependent average kinetic SVET-derived metal loss ($g.m^2$) for both flat and deformed surfaces is presented in Fig. 8. The data presented are the average value of two measurements. The solid line represents the flat surfaces, and the dotted line represents the 45° bend surfaces. For flat surfaces, GI and ZMA80 demonstrate a similar rate of metal loss for 1 h – 16 h. However, from the 16th hour onwards, the rate of corrosion for ZMA80 decreased compared to GI. The flat ZMA310 surface demonstrated significantly lower corrosion rate compared to GI and ZMA80. However, the corrosion rate increased linearly towards the end of the experiment (21 h–24 h).

The 45° bend surfaces of all three samples (GI, ZMA80 and ZMA310) demonstrated a relatively higher corrosion rate compared to their respective flat surfaces. However, this increase in corrosion rate was much greater in ZMA80 and ZMA310 compared to GI. The rate of corrosion for 45° bend surfaces of ZMA80 and ZMA310 increased gradually with respect to time; however, the rate of corrosion for GI was relatively constant.

The SVET-derived 24-hour cumulative metal losses for 45° bend surfaces along with flat surfaces of GI, ZMA80 and ZMA310 after

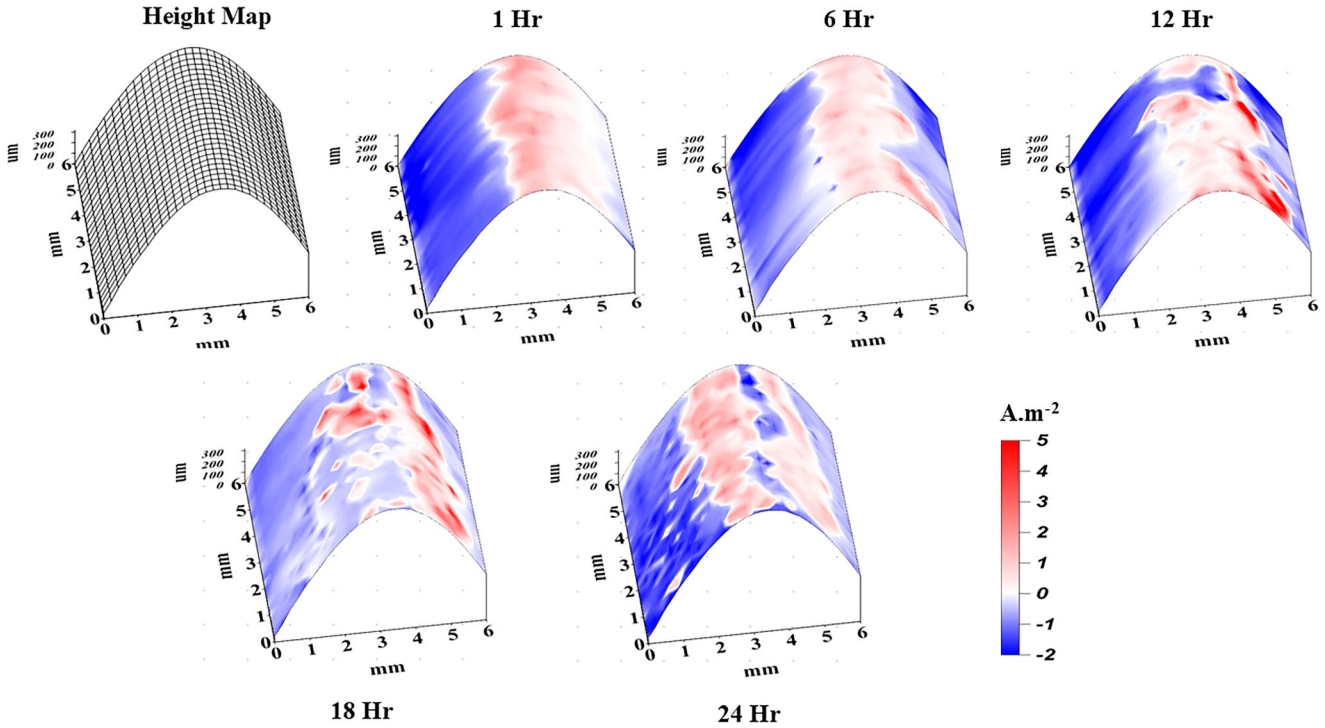

Fig. 5 | SVET colour maps representing normal current density measured above GI 45° bend surface in 0.17 M NaCl, pH 7 solution for 24 h. Anodic activity is displayed as red and cathodic activity as blue.

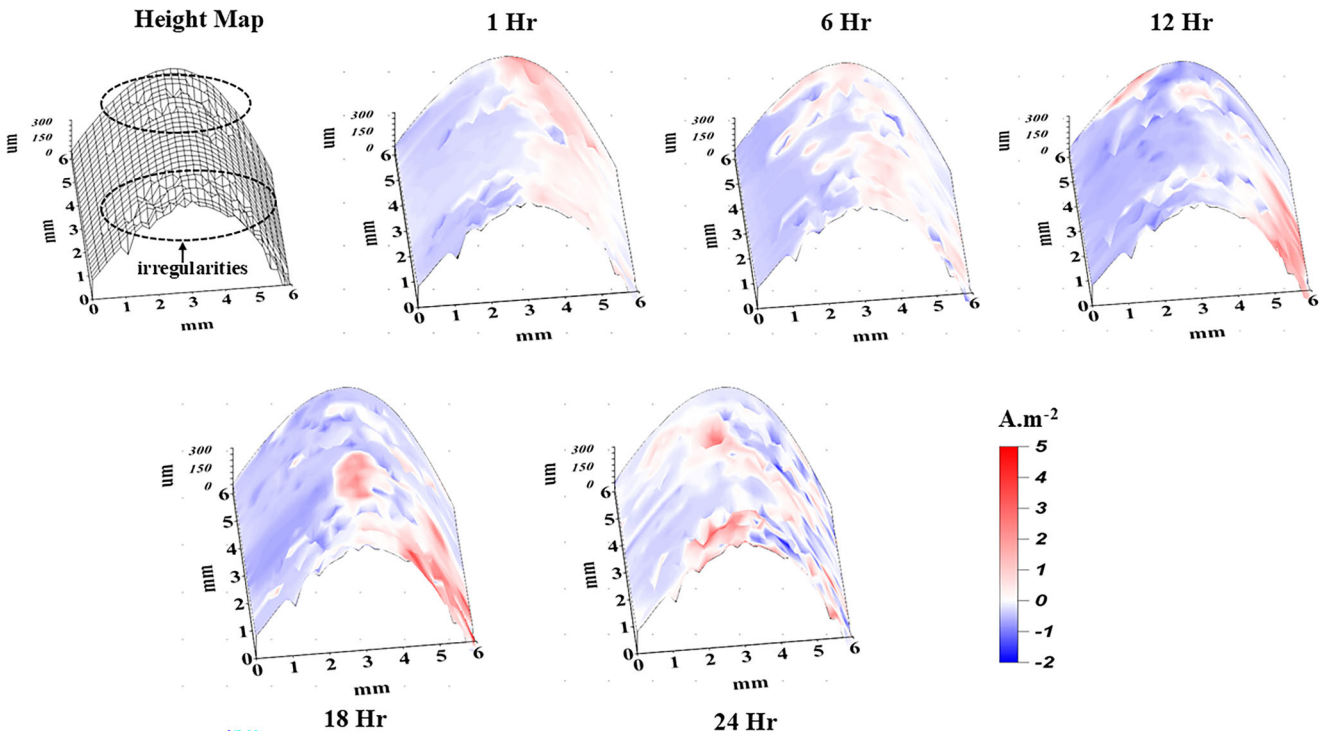

Fig. 6 | SVET colour maps representing normal current density measured above ZMA80's 45° bend surface in 0.17 M NaCl, pH 7 solution for 24 h. Anodic activity is displayed as red and cathodic activity as blue.

immersion in pH 7 0.17 M NaCl are presented in Table 5. The errors shown are based on the standard deviation of two measurements. The bent GI and ZMA310 surfaces demonstrated a similar metal loss, whereas ZMA80 demonstrated relatively higher metal loss compared to GI and ZMA310. The cumulative derived metal loss was 9.89 $g.m^{-2}$, 11.39 $g.m^{-2}$ and 9.17 $g.m^{-2}$ for 45° bend surfaces of GI, ZMA80 and ZMA310, respectively.

For each sample, the derived total metal loss increased when the sample was formed. The largest effect was observed for ZMA310, followed by ZMA80 and GI. For ZMA310, a proportional increase of 3.8 times was

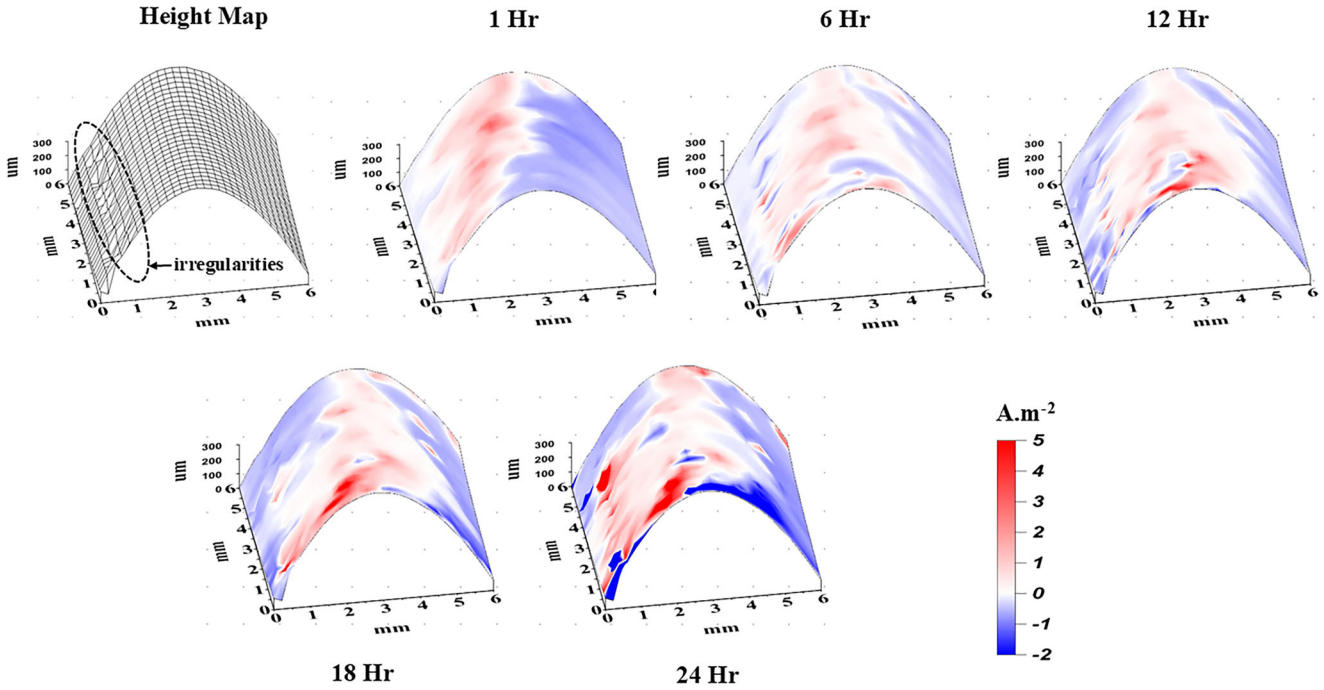

Fig. 7 | SVET colour maps representing normal current density measured above ZMA310's 45 ° bend surface in 0.17 M NaCl, pH 7 solution for 24 h. Anodic activity is displayed as red and cathodic activity as blue.

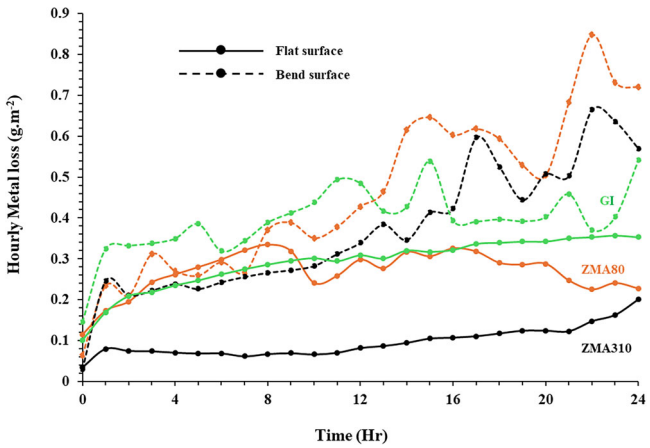

Fig. 8 | SVET measured time-dependent hourly metal loss for GI, ZMA80 and ZMA310 after immersion in 0.17 M NaCl pH 7 solution for 24 h. The solid line represents the flat surfaces, and the dotted line represents the 45° bend surfaces.

Table 5 | SVET-derived metal loss for flat and 45° bend surfaces of GI, ZMA80 and ZMA310 after immersion in 0.17 M NaCl pH 7 solution for 24 h

Sample	Flat Surface ($g.m^{-2}$)	45° Bend Surface ($g.m^{-2}$)	Average proportional increase in metal loss bend vs flat surface (times)
ZMA80	6.69 ± 1.75	11.39 ± 3.50	1.7
ZMA310	2.40 ± 1.15	9.17 ± 0.41	3.8
GI	6.74 ± 0.71	9.89 ± 0.34	1.5

observed. Similarly, a proportional increase of 1.7 times and 1.5 times was observed for formed ZMA80 and GI, respectively.

These kinetic differences were further analysed in Fig. 9, which shows the proportional change in SVET-derived hourly metal loss for 45° bend samples compared with flat. From Fig. 9, it was seen that GI had a relatively consistent increase in metal loss throughout the 24 h with a proportional increase of between one and two times (average = 1.5 times) for the bend surface. ZMA80 displayed a similar level of proportional increase in metal loss as GI up to 12 h. After 12 h, the value deviated upwards from the behaviour of GI with a peak increase in metal loss of 3.76 times at 22 h. ZMA310 demonstrated a consistently higher proportional increase in metal loss, with values increasing from three to four times those of the flat surface between 1 and 12 h, peaking at 5.4 times at hour 17. The final hour for ZMA80 and ZMA 310 exhibited a similar proportional increase of approximately three times that of the flat surface.

To further investigate the effects of deformation on the corrosion behaviour of ZMA and GI, open circuit potential (OCP) and linear polarisation resistance (LPR) experiments were performed. The time-dependent OCP values measured for GI, ZMA80 and ZMA310 immersed in a 0.17 M NaCl pH 7 solution for 24 h are presented in Fig. 10. The data presented are the average value of two measurements. The solid lines represent the flat surfaces, and the dotted lines represent the 45° bend surfaces for each respective sample. For ZMA80, forming the surface at a 45° angle shifted the hourly average OCP values to a more positive potential with an increase of ≈ 20 mV at the end of 24 h. However, the reverse was observed for the ZMA310 and GI, with a shift towards a more negative potential for the deformed samples. The shift of average hourly OCP to a more negative potential was much greater for ZMA310 (≈ 25 mV) compared to GI (≈ 6 mV).

The time-dependent LPR for GI, ZMA80 and ZMA310 immersed in a 0.17 M NaCl pH 7 solution for 24 h is presented in Fig. 11. The solid line represents the flat surfaces, and the dotted line represents the 45° bend surfaces. The LPR data have been presented as polarisation resistance (R_p) values and are indicative of the reciprocal of the rate of corrosion. The higher R_p indicates a lower corrosion current as $i_{corr} \propto 1/R_p$. In general, the LPR values decreased for the 45° bend surfaces compared to the respective flat surfaces. However, the most pronounced effect of the 45° bend was observed for ZMA310 as the difference in hourly average R_p values between the flat and the bend surfaces was significantly greater for ZMA310 compared to ZMA80 and GI. This is further illustrated in Fig. 12 that shows the

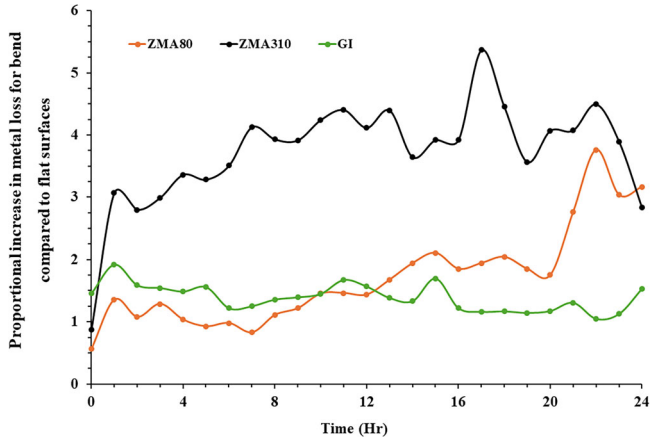

Fig. 9 | Average proportional increase in SVET-derived metal loss for bend surfaces compared to flat surfaces of GI, ZMA80 and ZMA310. The effect of deformation is greater on the ZMA compared to GI.

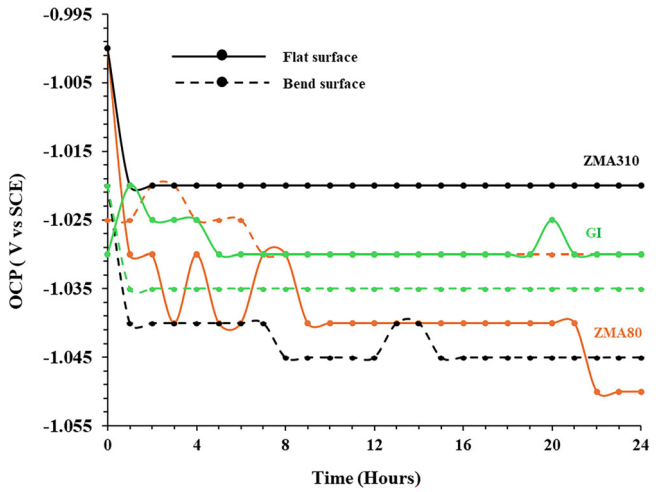

Fig. 10 | The time-dependent OCP measured for GI, ZMA80 and ZMA310 immersed in a 0.17 M NaCl pH 7 solution for 24 h. The solid line represents the flat surfaces, and the dotted line represents the 45 ° bend surfaces.

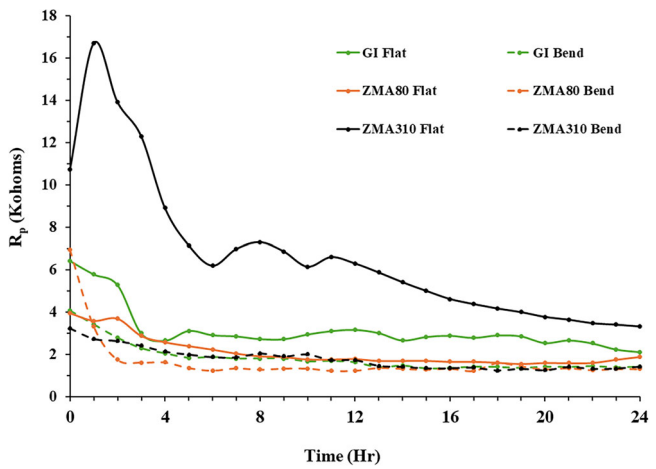

Fig. 11 | The time-dependent LPR for GI, ZMA80 and ZMA310 immersed in a 0.17 M NaCl pH 7 solution for 24 h. The solid line represents the flat surfaces, and the dotted line represents the 45 ° bend surfaces. The LPR values decreased for the 45° bend surfaces compared to the respective flat surfaces.

proportional decrease in R_p for each coating when comparing the LPR results of deformed surfaces with flat surfaces. The hatched line at a value of 1 is indicative of no proportional change in the LPR values between formed and flat surfaces. ZMA310 had an average decrease in LPR for the formed surface over 24 h of 3.6 times, peaking at 6.1 times after 1 h of electrolyte exposure. The LPR values generally decreased from the peak value down to the minimum over 24 h, with an arrest in this decrease occurring between 6 h and 17 h, where values varied around the average. ZMA80 had an average decrease in R_p for formed surfaces of 1.4 times, peaking at 2.1 times at 2 h, with a shallow decrease in rate up to 21 h, where the rate of change increased until the end of the experiment. GI had an average decrease of 1.8 times, peaking at 2.2 times at 13 h. Here, the decrease in R_p tended to become larger with respect to time, differing from the behaviour of the ZMA coatings.

Discussion

The HDG coatings ZMA80, ZMA310 and GI, when subjected to deformation, exhibited cracks around the tension radius of the bend (Figs. 2 & 3 and Table 3). However, the effect was significantly more pronounced on the ZMA coatings compared to GI. Cross-sectional images of 45° deformed ZMA80, ZMA310, and GI are presented in Fig. 13. The central region of the deformed coating was selected for the images as it experienced the greatest deformation.

Figure 13a shows a through-coating (cross-section) image of the GI surface after 45° deformation, and demonstrates limited damage to the coating with the formation of superficial micro-cracks of typical depth of ≈ 1 µm. However, for the multi-phase ZMA80 and ZMA310 coatings, 45° deformation caused greater damage, as large cracks, some even traversing through the entire coating to the steel substrate, were observed for both (Fig. 13 (b) – ZMA80 and Fig. 13 (c) – ZMA310). The susceptibility of ZMA coatings to cracking has been attributed to the presence of the binary eutectic phase ($Zn + MgZn_2$)[22]. It has been reported that cracks nucleate at the brittle intermetallic $MgZn_2$ present within the binary eutectic phase[22] which has a higher hardness and a lower strain hardening exponent[22]. Hence, the volume fraction and through-coating distribution of the eutectic phase present within the microstructure influence the number and size of cracks on the deformed ZMA coatings. Microstructural analysis revealed that changing the coating weight from 80 $g.m^{-2}$ (ZMA80) to 310 $g.m^{-2}$ (ZMA310) increased the volume fraction of the eutectic phase from 17.75 to 31.48% (Table 2) and the morphology of the primary zinc phase (Fig. 1). The reasons for the change in microstructure due to a change in coating thickness/weight have been explained previously[37,41]. The morphology of the primary zinc phase shown in the ZMA310 was dendritic, while the thinner ZMA80 coating exhibited a more globular primary zinc phase. The increase in binary eutectic phase volume fraction led to an increase in the area fraction of surface cracks in ZMA310 (9.6%) compared to ZMA80 (3.1%). Whereas the change in primary zinc shape (globular in ZMA80 to dendritic in ZMA310) has resulted in the formation of two types of cracks in ZMA310: through-coating (TC) cracks and non-through-coating (NTC) cracks. TC cracks were observed in both ZMA80 and ZMA310 (Fig. 13b, c), whereas NTC cracks were observed in ZMA310 only (Fig. 13d) and dominated in number along the deformed coating. The effect of microstructure on crack morphology is shown schematically in Fig. 14.

For ZMA80, the globular primary Zn phases traverse the entire thickness of the coating leaving direct pathways of eutectic from the surface to the steel substrate. Therefore, on deformation cracks can propagate rather easily along these pathways creating a through-coating crack (TC). For ZMA310, the dendritic structure tends to restrict direct pathways of eutectic from the coating surface to the steel substrate. Therefore, cracks that propagate from the surface are likely to encounter primary Zn dendrites that are considerably more ductile than $MgZn_2$ and hence, the primary zinc acts as a barrier/deflector for crack growth[22]. This leads to a situation where the coating is dominated by non-through coating cracks (NTC) with a limited amount of through-coating cracks developing where through-coating

eutectic pathways occur due to random growth of the microstructural phases.

The influence of coating weight/thickness on the corrosion mechanism of ZMAs has been reported previously[37,41] and therefore will not be discussed here. The corrosion experiments here showed that the 45° deformation influenced the corrosion behaviour of HDG ZMA and GI coatings. For deformed GI, a decrease in the OCP (Fig. 10) and an increase in the corrosion rate [LPR (Fig. 11) and SVET-derived metal loss (Table 5)] were observed. This decrease in OCP and increase in i_{corr} may occur from modifications to the anodic reaction, leading to anodic activation of the coating. This change in anodic behaviour can be explained by the differential aeration conditions induced by the geometry of the microcracks. A microstructural cross-section of the deformed GI (Fig. 13(a)) demonstrates the development of micro-cracks in the coating. These micro-cracks served as crevice sites, fostering a differential aeration environment that accelerated coating dissolution. A schematic of such a crack in the surface of the GI coating is shown in Fig. 15. Even though the cracks are relatively small, differences in O_2 diffusion to the surface of the coating and to the crack tip localised anodic activity at the crack tip and cathodic activity at the coating surface once the surface electrolyte became depleted of O_2 as per the Fontana-Greene mechanism of crevice corrosion[42]. Zn^{2+} is a weakly hydrolysable cation and as such an acidic pH develops at the crack tip where $Zn \rightarrow Zn^{2+} + 2e^-$. This is shown by the pink colour at the crack tip in Fig. 15. The cathodic oxygen reduction reaction (ORR) localised at the coating surface and at the crack entrance due to the ease of replenishment of oxygen at these regions and hence these regions became alkaline as $O_2 + 2H_2O + 4e^- \rightarrow 4OH^-$. This is shown as the regions of blue colour in Fig. 15. Migration of Zn^{2+} cations from inside the crack and OH^- anions from the cathode caused the formation of $Zn(OH)_2$ or Simonkolleite $Zn_5(OH)_8Cl_2$ corrosion products at the coating surface/crack entrance. The increase in cation concentration within the crack caused migration of Cl^- ions into the crack and therefore increased the corrosivity of the electrolyte. The combination of Cl^- influx and reduction in pH led to anodic activation at the crack tip and an increase in corrosion rate of around 1.5 times.

For deformed ZMA80, an increase in the OCP (Fig. 10), an increase in the corrosion rate [LPR (Fig. 11) and SVET-derived metal loss (Table 5)] were observed. This increase in both OCP and i_{corr} may occur from modifications to the cathodic reaction, leading to cathodic activation of the system. The microstructural cross-section image of the deformed ZMA80 (Fig. 13 (b)) reveals the formation of a TC-type crack within the coating, exposing the steel substrate. The mechanism of corrosion in this case is

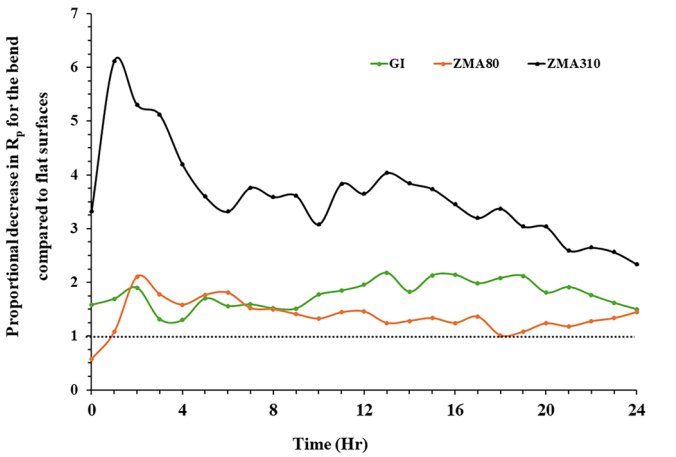

Fig. 12 | Average proportional increase in linear polarisation, R_p, for bend surfaces compared to flat surfaces of GI, ZMA80 and ZMA310. The effect of deformation is greater on the ZMA310 compared to GI and ZMA80.

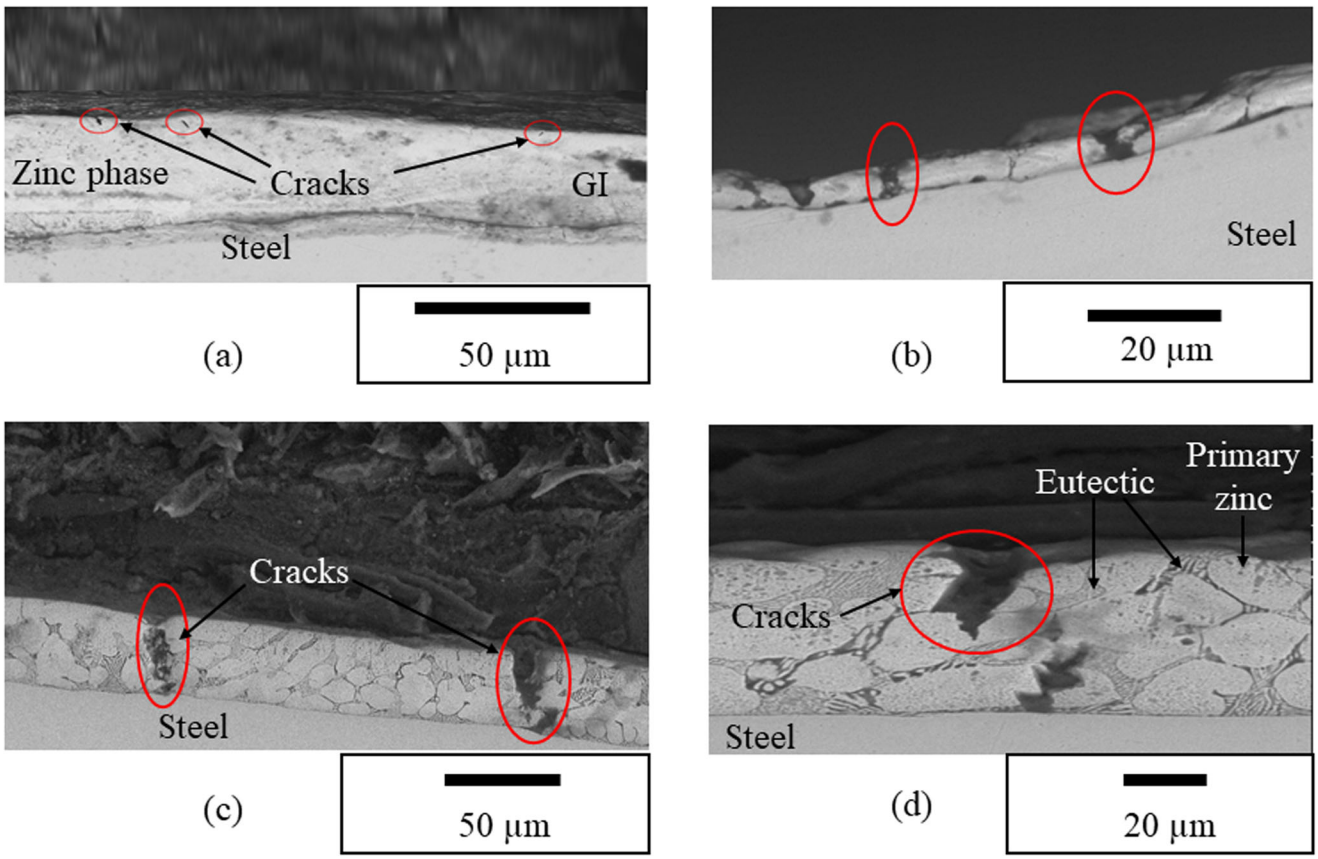

Fig. 13 | Images showing the cut-edge microstructure of HDG coatings post 45° deformation. The microstructures are for **a** GI **b** ZMA80 and **c**, **d** ZMA310. The images show the effect of 45° deformation on GI and ZMAs.

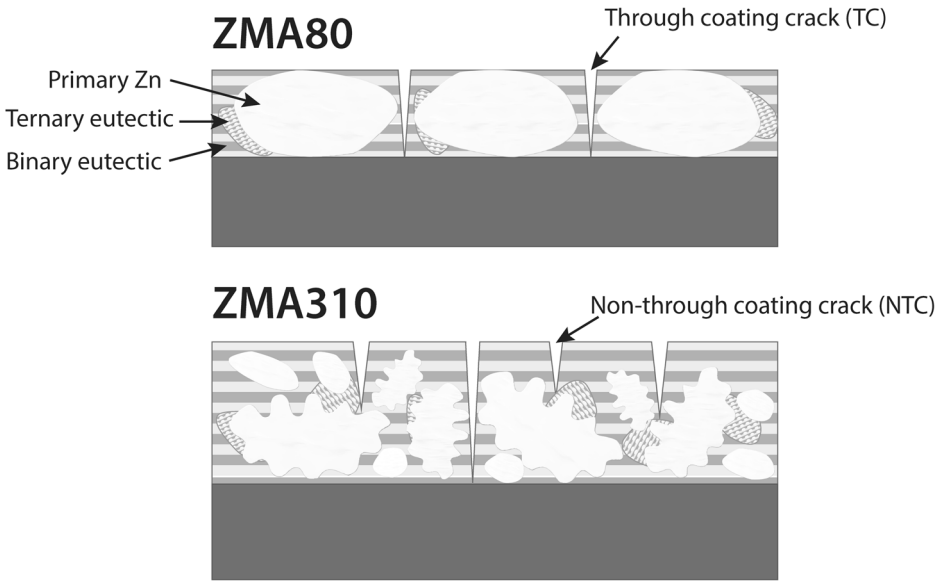

Fig. 14 | Schematic representation of ZMA coatings showing that changes to the morphology of the microstructure influence the depth of cracks on deformation to 45°. Though-coating cracks were present in both ZMA80 and ZMA310, whereas non-through-coating cracks were present in ZMA310 only.

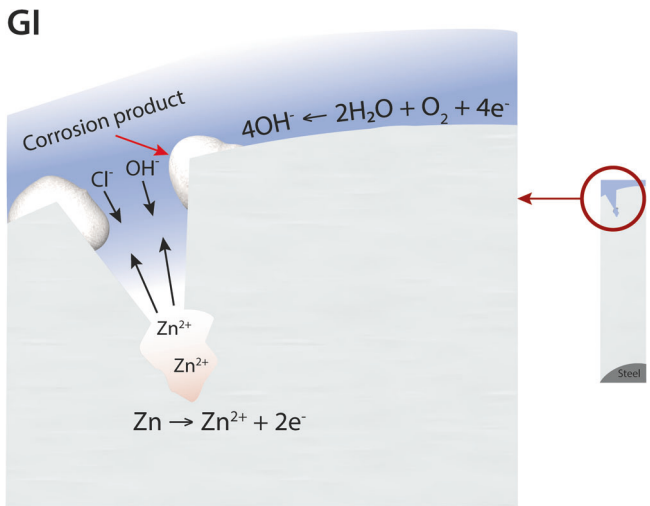

Fig. 15 | Schematic representation of the corrosion mechanism in the deformed GI surface. The image illustrates the establishment of a differential aeration corrosion mechanism due to the presence of microcracks in the surface of a deformed GI surface.

considered in Fig. 16 (a) and (b). A TC-type crack enabled the electrolyte to contact the steel substrate, and a galvanic couple formed between the ZMA80 coating and the steel. Hence, the system was cathodically activated, consequently accelerating the corrosion rate of the coating when compared to the undeformed surface. The increase in corrosion rate due to this galvanic coupling was between 1.5 - 2 times that of the undeformed surface, and this is because the area of steel exposed at each crack tip was relatively small leading to a relatively small increase in OCP (average 12 mV) and hence the increase in kinetics due to cathodic activation was low. Considering Fig. 16 (a), cathodic activity occurred at the base of the crack where the steel substrate was exposed. This created a region of alkalinity at the steel exposed at the tip of the crack. In this case, anodic metal dissolution occurred away from the crack tip with preferential release of Mg^{2+} and Zn^{2+} from $MgZn_2$, the most electrochemically active phase in the alloy[43]. The presence of Mg^{2+} and Zn^{2+} in the electrolyte tends to favour a less acidic pH near the anodic sites than for Zn^{2+} alone as Mg^{2+} does not readily hydrolyse. Cl^- migration into the crack from the bulk electrolyte tended to increase the corrosivity of the crack electrolyte. Migration of cations occurred towards the crack tip where the cathodic activity was located, and corrosion product formed once the solubility product of the corrosion product(s) is exceeded. The gradual build-up of corrosion products at the crack tip may eventually cover the exposed steel, deactivating the couple and leading to a mechanistic shift to that of differential aeration and anodic activation where the cathode now becomes located at the coating surface/crack entrance with the anode remaining within the crack as shown in Fig. 16b. As Mg^{2+} is depleted preferentially from the microstructure the transition to a Zn^{2+} dominated anolyte within the crack could again cause the pH to become acidic, migration of Cl^- would again occur into the crack, accelerating anodic dissolution within the crack and also potentially cause dissolution of the corrosion product "plug" at the crack tip that would again enable a galvanic couple to form. During the 24 hours of the experiments presented here, only net cathodic activation was observed, suggesting that galvanic coupling was the dominant accelerant of corrosion when ZMA80 was deformed.

The SVET-measured corrosion rate of deformed ZMA80 containing TC-type cracks was approximately 1.8 times higher than that of undeformed ZMA80 (Table 5 and Fig. 8). As indicated by the corrosion mechanism schematically illustrated in Fig. 16a, the equivalent metal loss derived from SVET for deformed ZMA80 at the early stages of exposure is likely underestimated. During this stage, anodic dissolution at the crack wall is galvanically coupled with the oxygen reduction reaction occurring on the exposed steel at the crack base. Because the SVET probe scans at a height of 100 µm above the corroding surface, the resulting anodic–cathodic current flux lines may not intersect the SVET scan plane and therefore remain undetected. In contrast, once the exposed steel becomes covered by corrosion products and the corrosion mechanism transitions to that shown in Fig. 16b, SVET detection is considerably more efficient.

For deformed ZMA310, a decrease in the OCP (Fig. 10) and an increase in the corrosion rate [LPR (Fig. 11) and SVET-derived metal loss (Table 5)] were observed. This decrease in OCP and increase in i_{corr} are again indicative of anodic activation of the coating. The microstructural cross-section image of the deformed ZMA310 (Fig. 13c, d) revealed the formation of both NTC as well as TC cracks through the eutectic regions. In contrast to the other two coatings, which exhibited superficial micro-cracks (NTC-type) on GI and TC cracks on ZMA80, ZMA310 exhibited both. Although the steel substrate was exposed, which cathodically activates the system as described for ZMA80, the presence of more numerous, large NTCs accelerated the anodic reaction and the system was net anodically activated as the OCP was decreased and i_{corr} was increased.

Figure 17 schematically shows a NTC crack in ZMA310. A differential aeration cell was established whereby anodic activity was localised

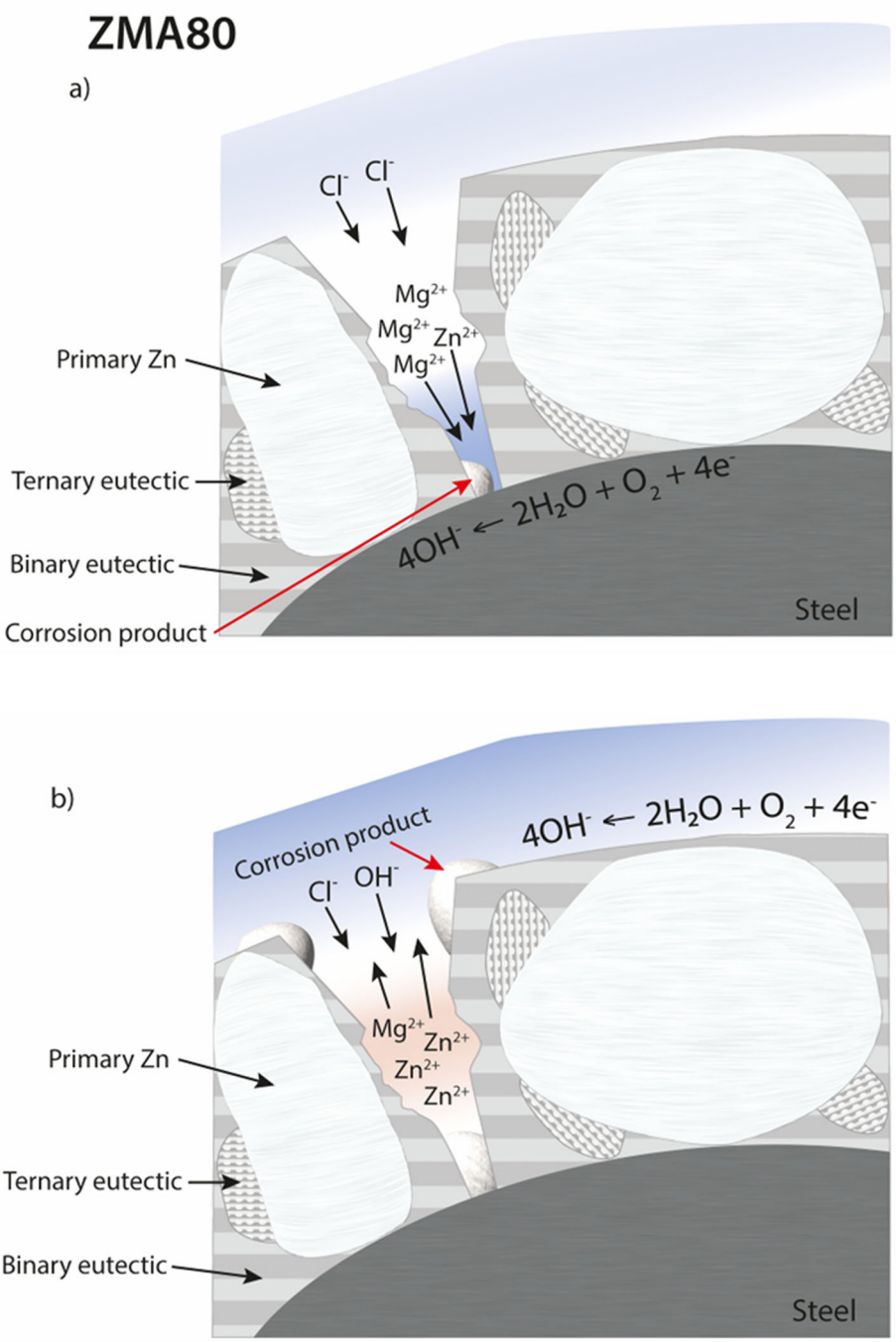

Fig. 16 | Schematic representation of different corrosion mechanisms established on the deformed ZMA80 surface. The images show **a** galvanic and **b** differential aeration corrosion mechanisms established over time due to the formation of through-coating cracks.

at the crack tip and the ORR was localised at the coating surface/crack entrance. The anodic attack was focused on $MgZn_2$ in the eutectic phases due to its potential of -1.41 V vs SCE compared to -1 V vs SCE for Zn. The Al phases were Al_2O_3 covered and are generally passive under the initial experimental conditions. The presence of Mg^{2+} cations in the crack electrolyte will tend to counter acidification due to Zn^{2+} hydrolysis, but some reduction in the pH may occur in the crack especially once the $MgZn_2$ is locally consumed and Zn^{2+} ions increase in concentration in the anolyte. Cl^- ions migrated into the crack increasing the corrosivity of the crack electrolyte. The localisation of the anode in the eutectic and the development of a higher concentration of Cl^- within the crack through differential aeration and the increased extent of cracking led to a significant increase in the corrosion rate of the coating. The increase in corrosion rate for deformed samples for ZMA310 was on average between 3 - 4 times for SVET measured metal loss and R_p values.

These data show that cracking is especially prevalent when ZMA coatings undergo deformation in comparison with GI and that the volume fraction of eutectic present in the ZMA is critical in determining the extent of cracking experienced during deformation with higher eutectic volume fractions leading to a greater area of cracking. Subsequently, the extent of cracking increases the corrosion rate of the system through anodic or cathodic activation through crevice corrosion and galvanic effects.

In conclusion, the effects of microstructural and deformation features on the corrosion behaviour of deformed and non-deformed surfaces of GI and ZMA coatings was systematically evaluated using a combination of techniques. The study demonstrates that;

- increasing the ZMA coating thickness from 80 $g{\cdot}m^{-2}$ (ZMA80) to 310 $g{\cdot}m^{-2}$ (ZMA310) induces a pronounced microstructural transformation. The morphology evolved from a fine globular structure to a

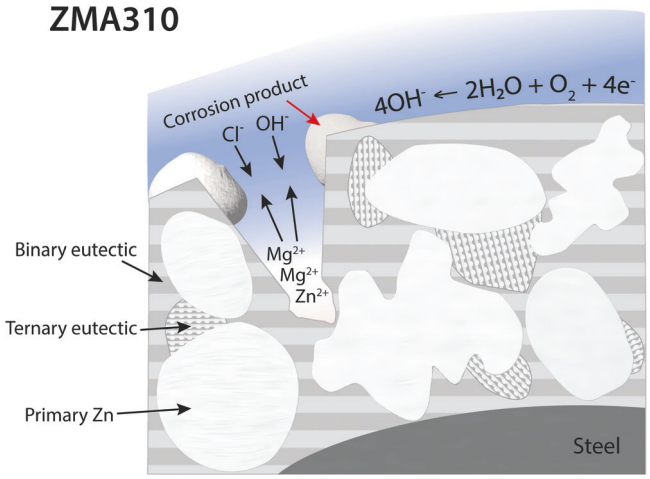

Fig. 17 | Schematic representation of the corrosion mechanism on the deformed ZMA310 surface. The image illustrates the establishment of a differential aeration corrosion mechanism due to the presence of a non-through coating crack in the surface of a deformed ZMA310 surface.

coarser dendritic structure, accompanied by a reduction in the primary Zn phase fraction from 82.25% to 68.52% and a corresponding increase in the eutectic phase fraction from 17.75% to 31.48%.

- ZMAs exhibited higher susceptibility to cracking during deformation, attributed to their complex multiphase microstructure. Surface crack analysis confirmed that the crack area increased with deformation angle (strain). At 45° deformation, ZMA310 displayed ~ three times greater crack area compared to ZMA80.
- Corrosion investigations (SVET & LPR) showed that surfaces formed to 45° of deformation significantly accelerated corrosion. The rate increase was most pronounced in ZMA310, followed by ZMA80 and GI. Relative to their flat surfaces, corrosion rates rose by 3.8 times (ZMA310), 1.7 times (ZMA80), and 1.5 times (GI).
- Deformed ZMA80 exhibited net cathodic activation, whereas GI and ZMA310 showed net anodic activation through galvanic coupling and crevice corrosion.

Methods

Materials

The GI (Zn-0.2 wt% Al) and ZMA [(1-2) wt% Al – (1-2) wt% Mg – Bal. Zn] coatings with different weights/thicknesses were produced on a continuous coil coating line. Processing parameters such as bath temperature and line speed were kept constant, whereas the gas knife pressure was altered depending on the produced coating weights. The thinner coatings require a closer knife-stripe distance and higher pressure compared to thicker coatings. A formable low-carbon steel (1.2 mm thickness) was used as the substrate and was coated on both sides.

Chemicals; hydrochloric acid (HCl), sodium hydroxide (NaOH), nitric acid (HNO_3) and ethanol (C_2H_5OH) were of analytical grade purity and purchased from Sigma-Aldrich Chemical Co. A 0.17 M NaCl pH 7 solution was used throughout, and the pH of the bulk solution was adjusted using aqueous NaOH or HCl.

Characterization

The samples were cut into 2 cm×2 cm coupons, mounted in a non-conductive resin (Metprep Ltd) and then polished with 1 µm diamond slurry (Metprep Ltd). Hitachi TM3000 Scanning Electron Microscope (SEM) with Burker Energy Dispersive X-ray Spectroscopy (EDS) module and digital optical microscope (Keyence VHX-7000 and Techno MT7100) were utilised to obtain microstructure images. The volume fraction of different microstructural phases was determined by cut-edge image analysis using Adobe Photoshop software.

A steel substrate coated with HDG coatings was cut into 20 mm×80 mm strips using shears. A Bayleigh BB-4816M-V2 Magnetic sheet brake was used to form the samples to the required angle. The plateau of the bend was used for surface crack analysis and corrosion experiments. For surface crack analysis, images taken at 50x magnification using a Keyence VHX-7000 digital microscope were analysed using the GNU Image Manipulation Program (GIMP 2.10) software. Both the image analysis software used were calibrated by setting a number of pixels to an already known measurement within the image.

Electrochemical measurements

OCP and LPR measurements were performed using Gamry Interface 1010E potentiostat. A platinum foil electrode and a saturated calomel electrode (SCE) were used as a counter and reference electrode respectively, to create a 3-electrode set-up. The samples were rinsed using deionised water and ethanol. An area of 36 mm^2 was exposed to the electrolyte. All experiments were carried out in 0.17 M NaCl, pH 7 over 24 hours. OCP was measured for 300 seconds, followed by a LPR measurement. During LPR measurements, samples were polarised by ± 15 mV from OCP at a scan rate of 0.166 mVs^{-1}. Although during the LPR measurement, the sample surface was polarised, the sample surface was allowed to stabilise before the next OCP measurement was taken. Measurements were taken every hour for 24 h and two tests were carried out for each material.

Scanning vibrating electrode technique (SVET)

The SVET was used to investigate the relative corrosion resistance/performance of the GI and ZMA coatings. For SVET experiments, a square area of 36 mm^2 (6 mm × 6 mm) masked off using 3 M non-conductive polytetrafluoroethylene (PTFE) tape was exposed to the electrolyte. 29 measurements were made along both the width and length of the exposed area, generating 841 data points for each scan. SVET has been extensively used for corrosion investigations for both planar and non-planar surfaces, whereas the instrument design and operation procedure can be found here[44–46]. In brief, SVET consists of a 125 µm diameter glass-encased platinum wire microtip vibrating perpendicularly at 100 µm above the corroding surface at a constant frequency of 140 Hz with an amplitude of 25 µm. The SVET detects the alternating potential at which the probe vibrates enabling monitoring of the temporal and spatial corrosion behaviour of the material. In addition, SVET enables the calculation of metal loss; however, it is considered semi-quantitative because multiple assumptions are made. The SVET metal loss calculation procedure is discussed in detail elsewhere, along with the SVET limitations[13,38,47,48]. For deformed surfaces, the non-planar or a 3-D SVET mode (Swansea Innovations, Swansea University, Wales, UK) was used. The map of the surface was generated by controlling the SVET tip position with a 3-dimensional orthogonal motor-driven linear array (Time and Precision Ltd, UK). Data logging and probe movement were controlled by a computer operated using in-house developed software (Swansea Innovations, Swansea University, Wales, UK)[40,49].

Data availability

The raw/processed data required to reproduce these findings cannot be shared at this time as the data also forms part of an ongoing study.

Received: 16 March 2026; Accepted: 21 April 2026;
Published online: 04 May 2026

References

1. Shah, S. R., Dilewijns, J. A. & Jones, R. D. The structure and deformation behavior of zinc-rich coatings on steel sheet. *J. Mater. Eng. Perform*. https://doi.org/10.1007/BF02646089 (1996).
2. Ploypech, S., Boonyongmaneerat, Y. & Jearanaisilawong, P. Crack initiation and propagation of galvanized coatings hot-dipped at 450°C under bending loads. *Surf. Coatings Technol.* **206**, 3758–3763 (2012).

3. Bastos, A. C., Ferreira, M. G. S. & Simões, A. M. P. Effects of mechanical forming on the corrosion of electrogalvanised steel. *Corros. Sci*. https://doi.org/10.1016/j.corsci.2012.11.026 (2013).
4. Sacco, E. A., Alvarez, N. B., Culcasi, J. D., Elsner, C. I. & Di Sarli, A. R. Effect of the plastic deformation on the electrochemical behavior of metal coated steel sheets. *Surf. Coatings Technol*. https://doi.org/10.1016/S0257-8972(03)00263-9 (2003).
5. Schürz, S. et al. Chemistry of corrosion products on Zn-Al-Mg alloy coated steel. *Corros. Sci.* **52**, 3271–3279 (2010).
6. Volovitch, P., Vu, T. N., Allély, C., Abdel Aal, A. & Ogle, K. Understanding corrosion via corrosion product characterization: II. Role of alloying elements in improving the corrosion resistance of Zn-Al-Mg coatings on steel. *Corros. Sci*. https://doi.org/10.1016/j.corsci.2011.03.016 (2011).
7. Prosek, T., Larché, N., Vlot, M., Goodwin, F. & Thierry, D. Corrosion performance of Zn–Al–Mg coatings in open and confined zones in conditions simulating automotive applications. *Mater. Corros.* **61**, 412–420 (2010).
8. Schuerz, S. et al. Corrosion behaviour of Zn-Al-Mg coated steel sheet in sodium chloride-containing environment. *Corros. Sci*. https://doi.org/10.1016/j.corsci.2009.06.019 (2009).
9. Chaouki, A. et al. Optimizing corrosion protection: Performance comparison of Zn and Zn-Al-Mg alloys Hot-Dip galvanized coatings. *J. Alloys Compd.* **1007**, 176371 (2024).
10. Malla, A. D. et al. The Effect of Germanium Additions on the Mechanical Properties of Zn-Mg-Al Alloys. *Metals (Basel)* **14**, 820 (2024).
11. Volovitch, P., Allely, C. & Ogle, K. Understanding corrosion via corrosion product characterization: I. Case study of the role of Mg alloying in Zn-Mg coating on steel. *Corros. Sci*. https://doi.org/10.1016/j.corsci.2009.03.005 (2009).
12. Duchoslav, J., Arndt, M., Keppert, T., Luckeneder, G. & Stifter, D. XPS investigation on the surface chemistry of corrosion products on ZnMgAl-coated steel. *Anal. Bioanal. Chem.* **405**, 7133–7144 (2013).
13. Wint, N. et al. The Effect of Microstructural Refinement on the Localized Corrosion of Model Zn-Al-Mg Alloy Coatings on Steel. *J. Electrochem. Soc.* **166**, C3147–C3158 (2019).
14. Britton, D. A. et al. Effect of antimony additions on the microstructure and performance of Zn–Mg–Al alloy coatings. *npj Mater. Degrad.* **8**, 62 (2024).
15. De Bruycker, E., Zermout, Z. & De Cooman, B. C. Zn-Al-Mg coatings: Thermodynamic analysis and microstructure related properties. in *Materials Science Forum* https://doi.org/10.4028/0-87849-428-6.1276 (2007).
16. Kim, D., Takata, N., Yokoi, H., Suzuki, A. & Kobashi, M. Microstructural factors controlling crack resistance of Zn–Al–Mg alloy coatings prepared via hot-dip galvanizing process: Combined approach of in-situ SEM observation with digital image correlation analysis. *J. Mater. Res. Technol*. https://doi.org/10.1016/j.jmrt.2024.01.235 (2024).
17. Švec, M., Nováková, I. & Solfronk, P. Determination of the Effect of Deformation on the Corrosion Resistance of Zn-Al-Mg Coated Sheets. *Manuf. Technol.* **23**, 709–716 (2023).
18. Ahmadi, M., Salgın, B., Kooi, B. J. & Pei, Y. Outstanding cracking resistance in Mg-alloyed zinc coatings achieved via crystallographic texture control. *Scr. Mater.* **210**, 114453 (2022).
19. Jaffrey, D., Browne, J. D. & Howard, T. J. The cracking of zinc spangles on hot-dipped galvanized steel. *Metall. Trans. B* **11**, 631–635 (1980).
20. Tzimas, E. & Papadimitriou, G. Cracking mechanisms in high temperature hot-dip galvanized coatings. *Surf. Coatings Technol.* **145**, 176–185 (2001).
21. Ahmadi, M., Salgın, B., Ahmadi, M., Kooi, B. J. & Pei, Y. Unraveling dislocation mediated plasticity and strengthening in crack-resistant ZnAlMg coatings. *Int. J. Plast.* **144**, 103041 (2021).
22. Ahmadi, M., Salgın, B., Kooi, B. J. & Pei, Y. Genesis and mechanism of microstructural scale deformation and cracking in ZnAlMg coatings. *Mater. Des.* **186**, 108364 (2020).
23. Ahmadi, M., Salgın, B., Kooi, B. J. & Pei, Y. The effect of grain refinement on the deformation and cracking resistance in Zn–Al–Mg coatings. *Mater. Sci. Eng. A* https://doi.org/10.1016/j.msea.2022.142995 (2022).
24. Prosek, T., Nazarov, A., Bexell, U., Thierry, D. & Serak, J. Corrosion mechanism of model zinc-magnesium alloys in atmospheric conditions. *Corros. Sci*. https://doi.org/10.1016/j.corsci.2008.06.008 (2008).
25. Sullivan, J. et al. In situ monitoring of corrosion mechanisms and phosphate inhibitor surface deposition during corrosion of zinc-magnesium-aluminium (ZMA) alloys using novel time-lapse microscopy. *Faraday Discuss*. https://doi.org/10.1039/c4fd00251b (2015).
26. Prosek, T. et al. Effect of the microstructure of Zn-Al and Zn-Al-Mg model alloys on corrosion stability. *Corros. Sci*. https://doi.org/10.1016/j.corsci.2016.04.022 (2016).
27. Sullivan, J., Mehraban, S. & Elvins, J. In situ monitoring of the microstructural corrosion mechanisms of zinc–magnesium–aluminium alloys using time lapse microscopy. *Corros. Sci.* **53**, 2208–2215 (2011).
28. Lee, J.-W. et al. Mechanistic study on the cut-edge corrosion behaviors of Zn-Al-Mg alloy coated steel sheets in chloride containing environments. *Corros. Sci.* **160**, 108170 (2019).
29. Duchoslav, J. et al. Structure and chemistry of surface oxides on ZnMgAl corrosion protection coatings with varying alloy composition. *Surf. Coatings Technol*. https://doi.org/10.1016/j.surfcoat.2019.04.006 (2019).
30. Persson, D., Thierry, D., LeBozec, N. & Prosek, T. In situ infrared reflection spectroscopy studies of the initial atmospheric corrosion of Zn-Al-Mg coated steel. *Corros. Sci*. https://doi.org/10.1016/j.corsci.2013.03.005 (2013).
31. Salgueiro Azevedo, M., Allély, C., Ogle, K. & Volovitch, P. Corrosion mechanisms of Zn(Mg,Al) coated steel: 2. The effect of Mg and Al alloying on the formation and properties of corrosion products in different electrolytes. *Corros. Sci*. https://doi.org/10.1016/j.corsci.2014.07.042 (2015).
32. Prosek, T., Persson, D., Stoulil, J. & Thierry, D. Composition of corrosion products formed on Zn-Mg, Zn-Al and Zn-Al-Mg coatings in model atmospheric conditions. *Corros. Sci*. https://doi.org/10.1016/j.corsci.2014.05.016 (2014).
33. He, X. et al. Influence mechanism of different elements and alloy phases on the corrosion resistance of Zn-Al-Mg coated steel in the atmospheric environment: A review. *Corros. Commun.* **13**, 49–59 (2024).
34. Guan, L. et al. Effects of U-Bending on Pitting Corrosion of 304L Stainless Steel. *Steel Res. Int*. https://doi.org/10.1002/srin.202000328 (2021).
35. Raja, V. S., Panday, C. K., Saji, V. S., Vagge, S. T. & Narasimhan, K. An electrochemical study on deformed galvanneal steel sheets. *Surf. Coatings Technol*. https://doi.org/10.1016/j.surfcoat.2006.03.044 (2006).
36. Vagge, S. T., Raja, V. S. & Narayanan, R. G. Effect of deformation on the electrochemical behavior of hot-dip galvanized steel sheets. *Appl. Surf. Sci*. https://doi.org/10.1016/j.apsusc.2007.04.045 (2007).
37. Malla, A. D. et al. Mechanistic investigation on the influence of coating weights on the corrosion behaviour of hot-dip-galvanised Zn-Mg-Al coatings. *npj Mater. Degrad.* **8**, 78 (2024).
38. Wint, N. et al. The ability of Mg2Ge crystals to behave as 'smart release' inhibitors of the aqueous corrosion of Zn-Al-Mg alloys. *Corros. Sci.* **179**, 109091 (2021).
39. Malla, A. D. et al. Influence of Mg and Al alloying additions on the corrosion mechanisms of Hot-dipped Zn-Mg-Al coatings: role of microstructure and phase distribution. *npj Mater. Degrad.* **9**, 96 (2025).

40. Wilson, B. P., Searle, J. R., Yliniemi, K., Worsley, D. A. & McMurray, H. N. Effect of probe tip inclination on the response of the Scanning Vibrating Electrode Technique to an idealised pit-like feature. *Electrochim. Acta* **66**, 52–60 (2012).
41. Penney, D. J., Sullivan, J. H. & Worsley, D. A. Investigation into the effects of metallic coating thickness on the corrosion properties of Zn–Al alloy galvanising coatings. *Corros. Sci.* **49**, 1321–1339 (2007).
42. Guy, F. M. *Corrosion Engineering*. (McGraw-Hill Education, 1985).
43. Ikeuba, A. I. et al. Understanding the electrochemical behavior of bulk-synthesized MgZn 2 intermetallic compound in aqueous NaCl solutions as a function of pH. *J. Solid State Electrochem*. https://doi.org/10.1007/s10008-019-04210-y (2019).
44. Worsley, D. A., McMurray, H. N. & Belghazi, A. Determination of localised corrosion mechanisms using a scanning vibrating reference electrode technique. *Chem. Commun*. 2369–2370 https://doi.org/10.1039/a704530a (1997).
45. Böhm, S., McMurray, H. N., Powell, S. M. & Worsley, D. A. Photoelectrochemical investigation of corrosion using scanning electrochemical techniques. *Electrochim. Acta* https://doi.org/10.1016/S0013-4686(99)00442-9 (2000).
46. Williams, G. & Neil McMurray, H. Localized Corrosion of Magnesium in Chloride-Containing Electrolyte Studied by a Scanning Vibrating Electrode Technique. *J. Electrochem. Soc.* **155**, C340 (2008).
47. Malla, A. D., Sullivan, J. H., Penney, D. J., Dunlop, T. & Barker, P. Mechanistic study on the corrosion behaviour of Zinc and Zinc-Calcium alloys designed for enhanced metallic coatings in the presence of chloride and phosphate ions. *Corros. Sci.* **213**, 110956 (2023).
48. Sheikholeslami, S. et al. Cut-edge corrosion behavior assessment of newly developed environmental-friendly coating systems using the Scanning Vibrating Electrode Technique (SVET). *Corros. Sci.* **192**, 109813 (2021).
49. Searle, J., Wilson, B., Yliniemi, K., Worsley, D. & Mcmurray, H. The Use of 3D-SVET for the Examination of Plasticized PVC Coatings: Effect of Deformation and UV Irradiation on Barrier Properties. *ECS Trans* **64**, 69–80 (2015).

Acknowledgements

We would like to thank the International Zinc Association and Swansea University for funding this work via the Galvanised Autobody Partnership program. This work was funded by Swansea University. For Open Access, the author has applied a CC By copyright licence to any Author Accepted Manuscript version arising from this submission.

Author contributions

A.D. Malla: Investigation, Methodology, Data curation, Formal analysis, Writing – original draft, Writing – review & editing, Validation. J.H. Sullivan: Conceptualization, Methodology, Validation, Formal analysis, Supervision, Writing – original draft, Writing – review & editing, Funding acquisition, Resources. D.J. Penney: Conceptualization, Methodology, Validation, Formal analysis, Supervision, Writing – original draft, Writing – review & editing, Funding acquisition, Resources. G. Williams: Writing – review & editing, Validation, Supervision, Resources. F.E. Goodwin: Writing – review, Resources. A.P. Cardoso: Writing – review, Resources. M. Brooks: Investigation, Methodology, Data curation.

Competing interests

The authors declare no competing interests.

Additional information

Correspondence and requests for materials should be addressed to A. D. Malla.

Reprints and permissions information is available at http://www.nature.com/reprints

Publisher's note Springer Nature remains neutral with regard to jurisdictional claims in published maps and institutional affiliations.